J Mater Sci: Mater Med (2009) 20:851–857
DOI 10.1007/s10856-008-3650-8

Study of the interfacial reactions between a bioactive apatite–mullite glass–ceramic coating and titanium substrates using high angle annular dark field transmission electron microscopy

Kenneth T. Stanton · Kevin P. O'Flynn · Shohei Nakahara · Jean-François Vanhumbeeck · John M. Delucca · Bobby Hooghan

Received: 23 September 2008 / Accepted: 3 November 2008 / Published online: 26 November 2008
© Springer Science+Business Media, LLC 2008

Abstract Glass of generic composition $SiO_2 \cdot Al_2O_3 \cdot P_2O_5 \cdot CaO \cdot CaF_2$ will crystallise predominantly to apatite and mullite upon heat-treatment. Such ceramics are bioactive, osseoconductive, and have a high resistance to fracture. As a result, they are under investigation for use as biomedical device coatings, and in particular for orthopaedic implants. Previous work has shown that the material can be successfully enamelled to titanium with an interfacial reaction zone produced during heat treatment. The present study uses high angle annular dark field transmission electron microscopy (HAADF-TEM) to conduct a detailed examination of this region. Results show evidence of complex interfacial reactions following the diffusion of titanium into an intermediate layer and the production of titanium silicides and titanium phosphides. These results confirm previously hypothesised mechanisms for the bonding of silicate bioceramics with titanium alloys.

K. T. Stanton (✉) · K. P. O'Flynn
School of Electrical, Electronic and Mechanical Engineering, University College Dublin, Belfield, Dublin 4, Ireland
e-mail: kenneth.stanton@ucd.ie

S. Nakahara
MSSI & Department of Physics, University of Limerick, Limerick, Ireland

S. Nakahara
Department of Electrical & Computer Engineering, Lehigh University, Bethlehem, PA 18015, USA

J.-F. Vanhumbeeck
Unité PCIM, Université Catholique de Louvain, Louvain-la-Neuve, Belgium

J. M. Delucca
LSI Corp., Allentown, PA, USA

B. Hooghan
Ovonyx Technologies Inc., 2956 Waterview Drive, Rochester Mills, MI 48309, USA

1 Introduction

Glass–ceramics were first produced by a French chemist, Réaumur, in 1739 who devitrified a glass to a polycrystalline material by heating it. However sufficient control over the process to create glass–ceramics in the modern sense eluded him [1]. S. D. Stookey in the early 50's, working at Corning Glass Works, was the first to use nucleation catalysts to manufacture glass–ceramics in a controlled manner [1]. Today, a wide range of glass–ceramics are available, fulfilling a variety of roles. Of particular interest here are glass–ceramics that are classed as bioactive.

Bioactive glass–ceramics have been developed for use in vivo both in restorative dental applications and bone implantation [2]. There are three main bioactive glass–ceramics: apatite–wollastonite developed by Kokubo et al. [3], mica-based developed by Grossman [4] and Beall et al. [5], and apatite–mullite [6, 7]. Calcium–phosphate based glasses and glass–ceramics have been investigated because their chemical composition resembles that of human hard tissue hydroxyapatite (HA, $Ca_{10}(PO_4)_6(OH)_2$) [8]. They are an alternative to the more commonly used synthetic hydroxyapatite for a number of reasons [7]. HA is usually applied via plasma-spraying but this is a line-of-sight process that results in a mixture of amorphous and crystalline phases with mixed dissolution rates [9]. The conventional sintering of HA can cause a reduction in strength of the final product as well as degradation of the HA into other calcium phosphate products [7]. Glass–ceramics are attractive because of their reproducible fine-grained microstructure

and the ability to control their properties through appropriate selection of composition and heat-treatment regime. The reactivity of a glass during processing is combined with the stability of a ceramic when finished if the material is applied as a glass to the substrate and subsequently crystallized in situ.

The subject of the present study is apatite–mullite glass–ceramics. These are materials that devitrify to form fluorapatite crystals ($Ca_{10}(PO_4)_6F_2$), which are a chemical analogue of the HA found in human teeth and bone [10], and mullite ($Si_2Al_6O_{13}$) which is inert but confers excellent mechanical strength. Apatite–mullite glass–ceramics have also been shown to be osseoconductive in vivo [11]. Fluorapatite is more chemically durable than its hydroxyapatite analogue and has a slower bioresorption rate [12, 13]. This occurs because of the difference in lattice strains produced by the OH^- hydroxyl ion and F^- ion. Unlike the OH^-, the F^- in the apatite lattice does not distort the hexagonal crystal structure due to its smaller size [14] and therefore produces a more stable crystal structure.

While it has been proven that glass–ceramics can be successfully enamelled to titanium substrates [15], little physical analysis has been carried out to examine the underlying chemistry or bonding mechanisms. Some authors have investigated the variation in elemental composition across the interface between bioactive glass coatings and titanium substrates, and have postulated possible reaction routes [9, 16, 17] but a similar comprehensive investigation has not been applied to bioactive glass–ceramics to date. In a previous examination into the bonding of apatite–mullite glass–ceramics to titanium, the coating interface was examined to determine the nature of the reactions occurring during bonding using high resolution TEM and selected area diffraction [18]. The reaction interface is relatively complex and the formation of titanium silicides (Ti_5Si_3, Ti_5Si_4 and $TiSi_2$) as interfacial reaction products were observed. The presence of these products in addition to the porosity in the interface was explained via reaction routes similar to:

$$5Ti + 3SiO_2 \rightarrow Ti_5Si_3 + 3O_2 \uparrow, \quad (1)$$

In the present study, a significantly more detailed investigation of the reaction interface was undertaken using high angle annular dark field transmission electron microscopy (HAADF-TEM) and energy dispersive x-ray analysis (EDX). HAADF-TEM operates by utilising Rutherford forward scattering—one of the many signals produced during the operation of a scanning transmission electron microscope—this is the interaction between electrons produced by the TEM and the atomic nuclei of the sample under investigation [19]. These scattered electrons emanate through a wide range of angles from the sample and HAADF-TEM utilises those at angles greater than 5° [19]. HAADF-TEM produces images whose intensities are approximately proportional to the atomic numbers of the atoms (Z) [20, 21] and has been successfully used, for example, to examine the glass/crystal interface in doped Si_3N_4 [22]. Due to the intensity proportionality, this is a useful imaging tool for the investigation of interfaces where a significant difference between the atomic weights of the constituent elements exists. Otten has shown that HAADF can be up to 10^5–10^6 times more sensitive than energy-dispersive X-ray spectroscopy [19].

Here we use an apatite–mullite glass–ceramic coating enamelled onto two titanium substrates—Ti6Al4V and TMZF. Ti6Al4V is a biphasic alpha–beta alloy frequently used in vivo. TMZF ($TiMo_{12}Zr_6Fe_2$) is a relatively new alloy developed by Stryker Howmedica in 1998. It has the advantage of producing less debris during wear testing than Ti6Al4V [23]. Whereas titanium has an α structure at room temperature, TMZF retains a β structure due to the presence of the β-stabilisers molybdenum, zirconium, and iron. The β phase of titanium has a significantly lower modulus of elasticity than the α phase [24], giving it "flexibility, strength and resistance to corrosion and ductility… TMZF is 25% more flexible than the well studied Ti6Al6V4 alloy" [23]. Ti6Al4V is a common biomedical grade alloy used for structural orthopaedic applications. It was used to examine the coating-substrate interface using HAADF-TEM. TMZF was used to examine oxygen infiltration into the substrate because oxygen is an α stabilizer and therefore produces an α phase in an otherwise β material, allowing observation by optical microscopy.

2 Materials and methods

2.1 Glass synthesis

The glass system used has the generic composition of $1.5(5 - x)SiO_2 \cdot (5 - x)Al_2O_3 \cdot 1.5P_2O_5 \cdot (5 - x)CaO - xCaF_2$, where x can vary between 0.5 and 2.0. This system has previously been examined with detailed thermal and X-ray analysis [25, 26] and is designed to maintain an apatitic Ca:P ratio of 1.67. Two glasses were used for the present study—a high fluorine glass called JFG1 with $x = 1.87$ as it produces a high apparent nucleation density with bulk nucleation prevalent [15], and an intermediate fluorine content glass, LG27 with $x = 1$, which has a lower nucleation density. Fluorine acts as a network modifier, lowering the crosslink density [27], increasing atomic mobility, and lowering the glass transition and crystallization temperatures. The reagents were mixed for 40 min in a ball mill without P_2O_5 due to the hygroscopic nature of the latter component. The P_2O_5 was then added and the

mixture ball-milled for a further 15 min. The powder was then placed into a high density lidded mullite crucible. Using an electric furnace, the crucible and charge were heated to 1,400°C and held at this temperature for 2 h. The glass melt was then poured directly into demineralised water to shock quench it to room temperature, thereby avoiding crystallization and preserving the amorphous nature of the glass. The resultant glass frit was oven dried in air for one day before grinding and sieving to give a particle size of <45 μm.

2.2 Differential scanning calorimetry (DSC)

DSC was performed using a Rheometric Scientific STA 1600 (Surrey, UK) to determine the crystallization temperatures. A flowing dry nitrogen atmosphere with a heating rate of 10°C min^{-1} was used.

2.3 X-ray diffraction (XRD)

Powder XRD was performed to confirm that the glass was initially fully vitreous and, when heated to above T_{p2}, fully crystallized to apatite and mullite with minimal residual glass. Prior to XRD, the sample was crystallized by heating in a muffle furnace at 10°C min^{-1} and quenched in air to room temperature after reaching the target temperature so as to mimic the DSC experiment conditions. Analysis was carried out in a Huber 642 Guinier Diffractometer (Rimsting, Germany) with a quartz Johansson monochromator and copper target operating in subtractive transmission mode at 50 kV and 25 mA. X-rays were pure monochromatic CuKα_1 with $\lambda = 1.54056$Å. A silicon internal standard was used to allow non-linear peak shift correction.

2.4 Glass enamelling procedure

The coating was deposited on the substrates using a simple sedimentation route. Glass powder of <45 μm was mixed with ethanol to create a slurry. This was poured onto the substrate and ultrasonic agitation was used for 3 min to give a homogeneous layer and to break-up any powder aggregates. The sample was placed in a vacuum oven at 120°C for 24 h to dry. It was then heat treated in vacuo in a muffle furnace under the following conditions: from room temperature at 10°C min^{-1} to 670°C (the optimum nucleation temperature [15]); held for 60 min; 670°C to 960°C at 10°C min^{-1}; held for 90 min; cool to ambient at 10°C min^{-1}. This heating regime is based on the DSC data and designed to fully devitrify the glass–ceramic and enamel it to the substrate without heating above the $\alpha \rightarrow \beta$ transition (970°C) for Ti6Al4V which could affect the fatigue properties of the metal [25]. While T_{p2} (997°C) was not reached, 960°C is above the mullite crystallization onset temperature of 938°C and would be expected to produce a fully crystallized material following the hold for more than one hour. The glass system has a thermal expansion coefficient similar to that of Ti6Al4V [15] so delamination did not occur. After cooling, the coating proved to be well adhered to the Ti6Al4V with no cracking evident and could not be removed by scratching with a thumbnail (detailed mechanical testing will be carried out in a separate study). The subsequent interfacial reaction was examined using high angle annular dark field transmission electron microscopy (HAADF-TEM).

2.5 High angle annular dark field transmission electron microscopy (HAADF-TEM)

Transmission electron microscopy was performed using an FEIs TECNAI 20F FEG TEM/STEM microscope equipped with an EDAX energy dispersive X-ray (EDX) detector. The microscope was operated at an accelerating voltage of 200 keV. TEM specimens were prepared using the standard focused ion beam (FIB) lift-out technique.

2.6 Optical microscopy

For optical microscopy, the samples were mounted in a 30 mm diameter Bakelite disc before being ground and polished to a 1 μm finish. To reveal the microstructure, the sample was first dipped in a solution of 10 ml KOH (40%), 5 ml H_2O_2 (30%) and 20 ml of H_2O for 5 s, then concentrated HF for 1 s and finally immersed in a solution of 10 ml HF, 5 ml of HNO_3, and 85 ml H_2O for 10–15 s, before being rinsed with water, then alcohol and finally acetone. A Leica MEF4 M optical microscope was used to image the samples with reflected light.

3 Results and discussion

DSC analysis shows the existence of two crystallization exotherms in both glasses with peak temperatures: T_{p1} at 783°C for JFG1 and 899°C for LG27 corresponding to apatite and T_{p2} at 997°C for JFG1 and 1,001°C for LG27 corresponding to the crystallization of apatite & mullite together, see Fig. 1 [26, 28]. The optimum nucleation temperature, defined as the temperature at which the greatest number of stable nuclei form per volume element, has been reported elsewhere as 670°C for JFG1[15]. Both glasses crystallize to form apatite–mullite glass–ceramics although the increased amount of fluorine, a network disruptor, in JFG1 has deceased the glass-transition temperature and peak crystallization temperatures.

Powder XRD confirmed that both glasses were initially vitreous and, when heat-treated to 1,200°C, crystallized to

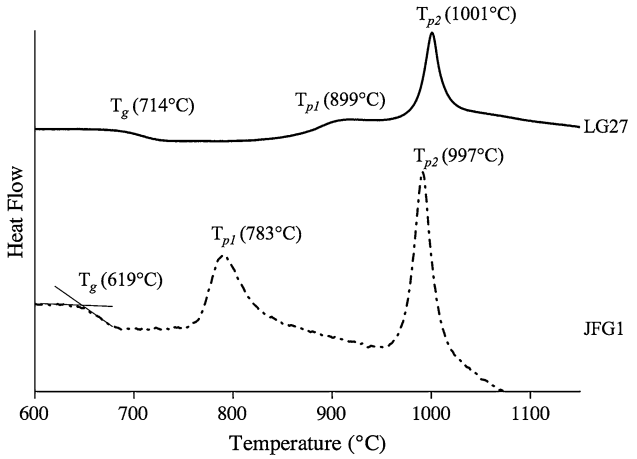

Fig. 1 DSC traces of JFG1 and LG27 showing T_g onset and two crystallization exotherms, T_{p1} (crystallization of apatite) and T_{p2} (apatite and mullite)

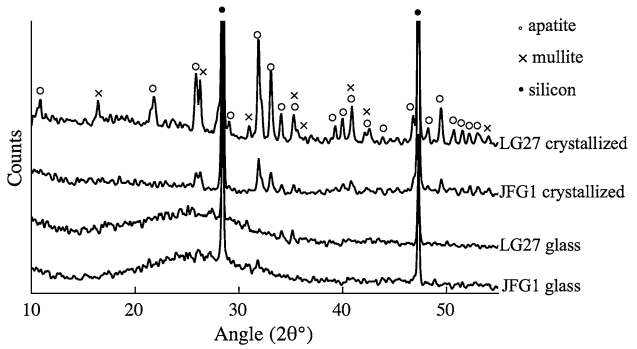

Fig. 2 XRD of JFG1 and LG27 before and after devitrification at 1,200°C. In both glass samples, the amorphous halo between 14 and 37° (2θ) is indicative of a pure glass phase. The 1,200°C samples have sharp peaks with no halo, proving the existence of apatite and mullite in a fully devitrified sample with minimal residual glass. A silicon internal standard was used

form apatite and mullite with little residual glass, see Fig. 2.

The apatite–mullite glass ceramic JFG1, the principle subject of this investigation, proved to be well adhered to the titanium substrate indicating that a successful reaction had occurred. There was no delamination due to the similarity between thermal expansion coefficients of coating and metal [15].

Figure 3 shows images of the sample after FIB milling. The Ti6Al4V substrate appears on the left in region a, the interfacial reaction region in region b, and the homogeneous apatite–mullite coating in region c. Two voids are evident as large black regions in the middle of the sample in the HAADF image. These could have been produced during the substrate-coating reaction, the ion beam milling process or a combination. Analysis was avoided near these voids as a layer-like structure containing a high concentration of

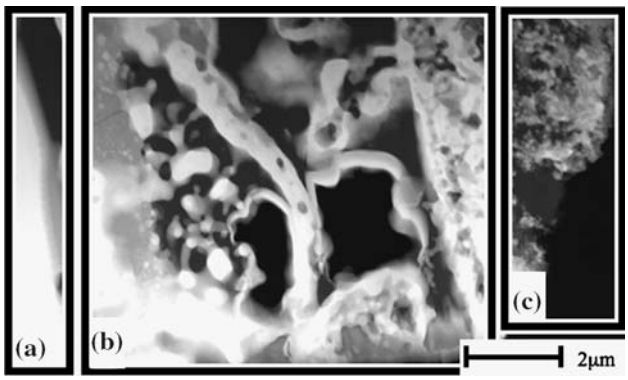

Fig. 3 High angle annular dark field transmission electron microscope image of the sample showing three separate areas—a is the Ti6Al4V substrate, b is the interfacial reaction zone, and c is the homogeneous apatite–mullite coating

gallium was found and it is likely that some carbonaceous material also redeposited during focused-ion-beam cutting.

Figure 4 shows both bright field, 4(i), and high angle annular dark field, 4(ii), transmission electron microscope images of the sample. There are three distinct regions evident. The titanium substrate is on the very left of the images and appears bright in the HAADF image due to atomic number (Z) contrasting. The apatite–mullite coating is on the right. Figure 4a shows an enlarged image of the coating where the presence of nano-scale crystals, similar to those observed during previous investigations [29], can be seen. The crystals appear to have grown in a banded structure consistent with amorphous phase separation prior to crystallization via spinodal decomposition. The crystals can be seen in greater detail when a lower fluorine content glass is crystallized (LG27, $x = 1$). A lower fluorine content glass has a diminshed network connectivity and hence a reduced nucleation density, allowing the crystals to grow to a larger size that can be easily seen. The crystals can be seen in Fig. 5. It is likely that some residual glass exists within this region also.

In the intervening 10 μm between the metal and glass–ceramic is a complex interfacial reaction region. To determine the nature of the reactions, the resultant products were identified using two electron microprobe analysis (EDX) methods: spot and line analysis. The results reveal that significant atomic diffusion occurred, between both the coating and substrate.

Considering first the coating, Fig. 4b and c show enlarged images of areas within the reaction region, along with associated EDX data. An elemental analysis of the regions show the dominant presence of titanium, silicon and phosphorous. It is proposed that two particular compounds, titanium silicides and titanium phosphides, exist in segregated regions within this area. The lack of significant vanadium diffusion is expected since it comprises only 4 wt.% of the metal substrate.

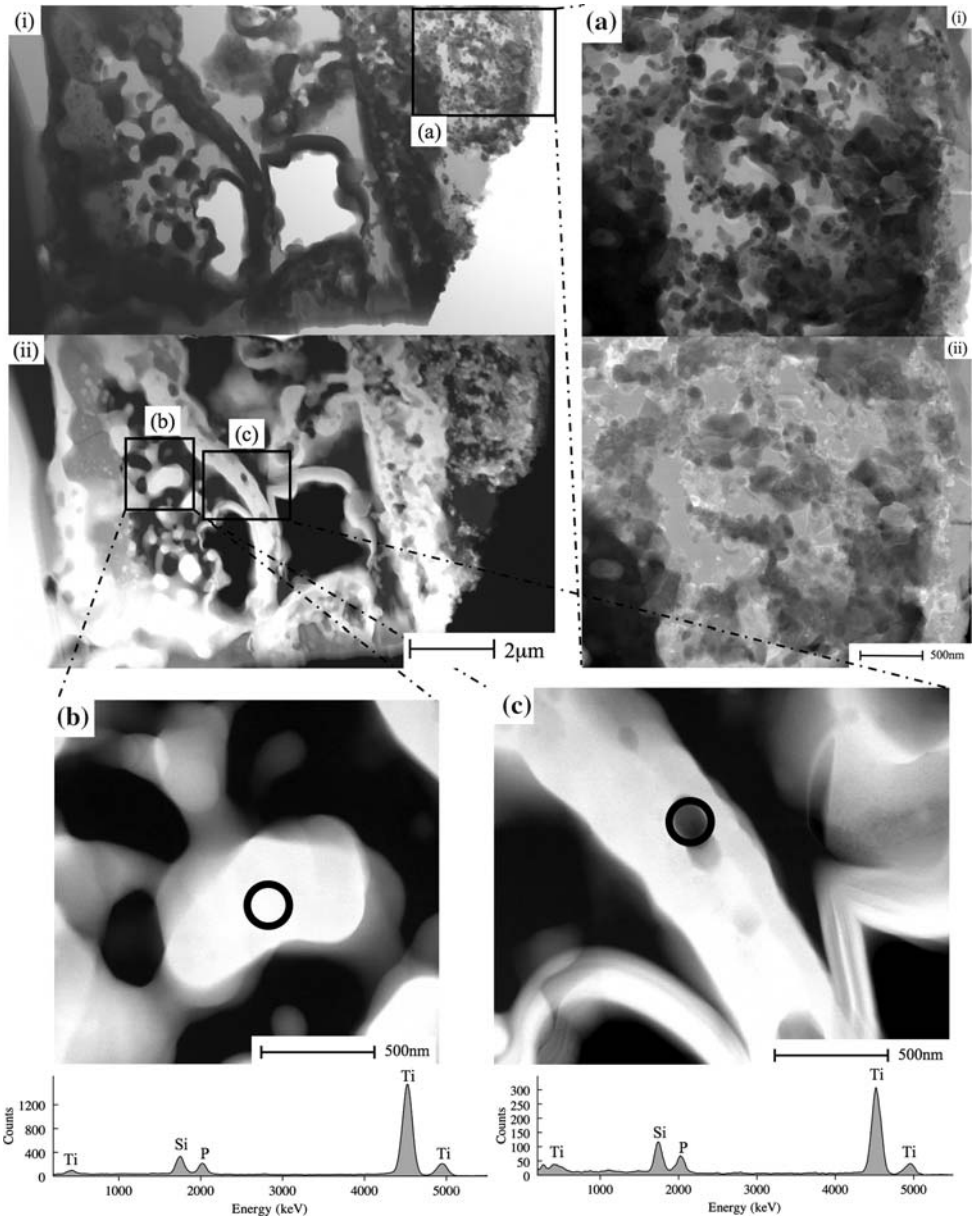

Fig. 4 Bright field, (i), and high angle annular dark field, (ii), transmission electron microscope images of the sample showing the edge of the substrate on the left appearing bright in (ii) because of the atomic number contrasting. Enlarged images are shown of areas (**a**), (**b**) and (**c**). **a** shows apatite–mullite nanocrystals in both bright field, (i), and dark field imaging, (ii),. They show a banded nature consistent with having undergone amorphous phase separation prior to crystallization. **b** and **c** show respective spots and EDX spectra indicating the presence of titanium silicides and titanium phosphides

A line spectrum was used to examine the variation of these products across a wider area and the results are shown in Fig. 6. The microscopy image displays the region through which the analysis was conducted. The spectrum is split into two areas, the substrate (i) and the interfacial region (ii). Although the titanium substrate should have a negligible concentration of oxygen, it can be observed that oxygen diffusion has occurred into the substrate during sintering. This would be expected to lead to oxygen embrittlement of the titanium. To examine the oxygen infiltration more closely, a pure β alloy, TMZF, was enamelled with an apatite–mullite coating. Oxygen is an α stabiliser and, when the α phase is etched away, the diffusion paths become evident. Figure 7 is an optical micrograph of this effect showing oxygen diffusion along preferential crystallographic directions and grain boundaries of the substrate. The line spectrum of the interfacial reaction region spectrum shows the variation in atomic percent of titanium, phosphorous and silicon. There is a definite correlation between the different elements in certain regions: an apatite–mullite material region with little titanium and other areas of titanium silicides and titanium phosphides. Previous work with bioactive glasses has suggested certain reaction routes between bioactive glasses and titanium and similar reactions were observed to have occurred for apatite–mullite glass–ceramics. The formation of titanium silicides has been proposed to occur via two different routes: one by Tomsia and Pask for sodium silicate glasses on Ti in an inert atmosphere [30]:

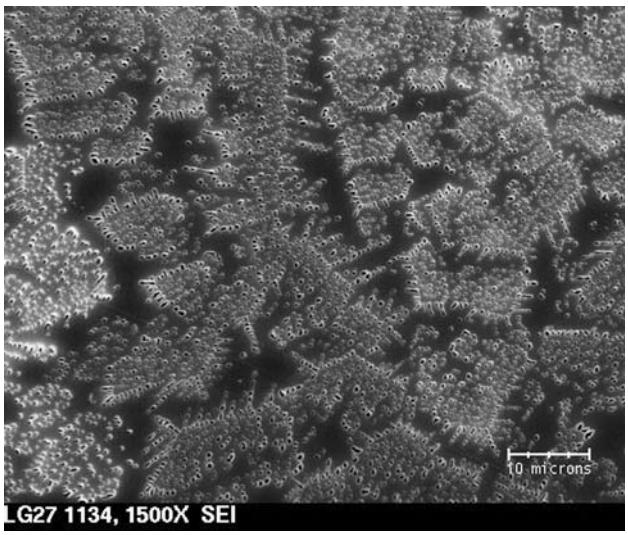

Fig. 5 Backscattered electron image of LG27 ($x = 1$) showing larger apatite crystals

$$8Ti + 3SiO_2\{glass\} \rightarrow Ti_5Si_3 + 3TiO_2\{glass\} \quad (2)$$

and the other by Hang and Holland for lithium–alumino–silicate glass–ceramics on Ti in argon [31]:

$$5Ti \rightarrow 3SiO_2 \rightarrow Ti_5Si_3 + 3O_2 \uparrow \quad (3)$$

Gomez-Vega et al. list three possible routes for the production of titanium phosphides [9, 31, 32]:

$$16Ti + 6P_2O_5 \rightarrow 4Ti_4P_3 + 15O_2 \uparrow \quad (4)$$

$$9Ti + 3P_2O_5 \rightarrow 2Ti_4P_3 + 7O_2 \uparrow + TiO \quad (5)$$

$$17Ti + 6P_2O_5 \rightarrow 4Ti_4P_3 + 14O_2 \uparrow + TiO_2 \quad (6)$$

Little evidence for the presence of the amount of titanium oxide required by routes (2), (5), and (6) was found. Figure 6 shows the variation of oxygen and titanium in the interfacial region. It can be seen that there is little correlation in a manner that suggests the production of titanium oxides in association with that of titanium silicides and titanium phosphides. It must therefore be assumed that reactions (3) and (4) are the more likely. This conclusion is supported by work done by Stanton et al. [18]. The release of O_2 associated with this reaction may also explain the significant oxygen diffusion into the substrate and the formation of voids discussed earlier.

4 Conclusions

Enameling is an effective technique for the coating of titanium substrates with apatite–mullite glass–ceramics. A complex interfacial reaction zone is formed during the bonding with the production of titanium silicides via the reaction route:

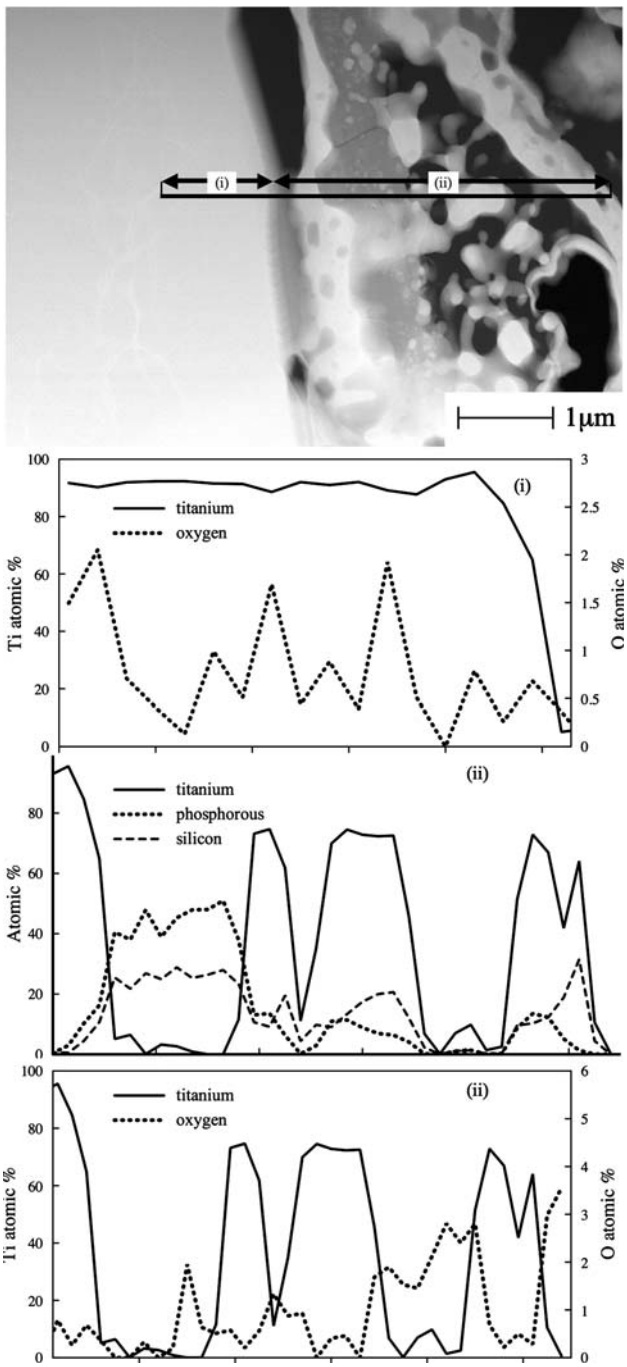

Fig. 6 EDX line spectrum analysis, showing the levels of titanium & oxygen content in the substrate in (i), and titanium, phosphorous & silicon, and titanium & oxygen in the interfacial reaction region (ii). There is a correlation between the levels of titanium, phosphorous & silicon in certain regions whereas the same relationship between titanium & oxygen is not observed, implying reaction routes (3) and (4) are most likely. The presence of oxygen in the substrate indicates that oxygen diffusion occurred during the reaction

$$5Ti + 3SiO_2 \rightarrow Ti_5Si_3 + 3O_2 \uparrow \quad (7)$$

and titanium phosphides via:

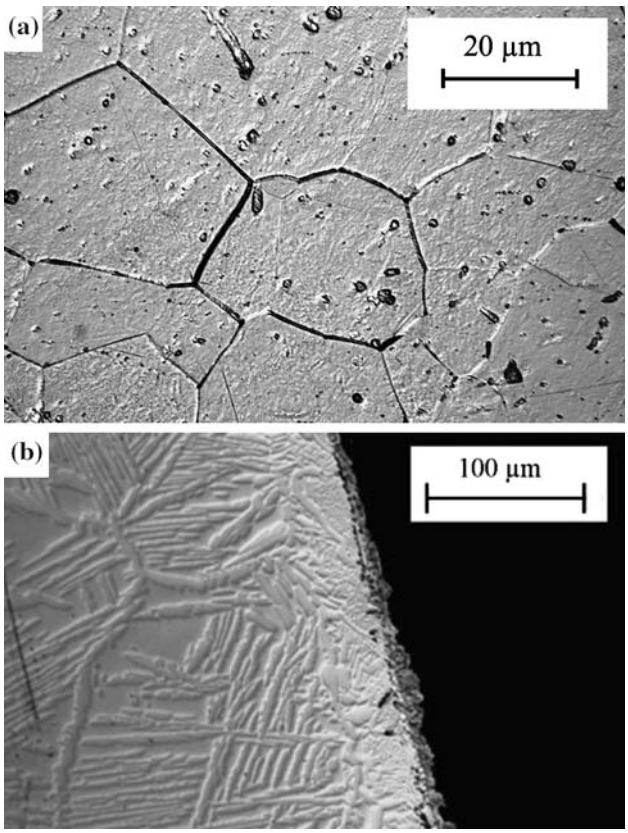

Fig. 7 Optical microscopy image of TMZF pre- and post-heat treatment. The pre-heat treated microstructure is shown in (**a**) and is uniform. The oxygen diffusion paths along preferential crystallographic directions and grain boundaries through sintered TMZF can be seen in (**b**) where they were preferentially etched by the same solution used for (**a**)

$$16\mathrm{Ti} + 6\mathrm{P_2O_5} \rightarrow 4\mathrm{Ti_4P_3} + 15\mathrm{O_2} \uparrow \quad (8)$$

However it must be noted that significant oxygen infiltration into the substrate did occur during sintering.

Acknowledgements The authors wish to acknowledge the assistance of Dr. Alun Carr at University College Dublin for his assistance with the X-ray diffraction experiments. Part funding was provided by the Irish Research Council for Science, Engineering and Technology: funded by the National Development Plan.

References

1. P.W. McMillan, *Glass-ceramics* (Academic Press, New York, 1964)
2. W. Höland, J. Non-Cryst. Solids **219**, 192–197 (1997). doi:10.1016/S0022-3093(97)00329-3
3. T. Kokubo, M. Shigematsu, Y. Nagashima, M. Tashiro, T. Nakamura, T. Yamamuro et al., Bull. Inst. Chem. Res. Kyoto Univ. **60**, 260–268 (1982)
4. US Patent No 3839055 (1974)
5. G. Beall, M. Montierth, G. Smith, Microtecnic. **42**, 173 (1972)
6. R. Hill, D. Wood, J. Mater. Sci. Mater. Med. **6**(6), 311–318 (1995). doi:10.1007/BF00120298
7. A. Clifford, R. Hill, J. Non-Cryst. Solids **196**(1–3), 346–351 (1996). doi:10.1016/0022-3093(95)00611-7
8. T. Kasuga, M. Nogami, M. Niinomi, Key Eng. Mater. **192–195**, 223–226 (2001)
9. J. Gomez-Vega, E. Saiz, A. Tomsia, J. Biomed. Mater. Res. **46**(4), 549–559 (1999). doi:10.1002/(SICI)1097-4636(19990915)46:4<549::AID-JBM13>3.0.CO;2-M
10. R. Bowen, J. Dent. Res. **44**(5), 906–911 (1965)
11. C. Freeman, I. Brooks, A. Johnson, P. Hatton, R. Hill, K. Stanton, J. Mater. Sci. Mater. Med. **14**, 985–990 (2003). doi:10.1023/A:1026306901058
12. H. Kim, B. Yoon, Y. Koh, H. Kim, J. Am. Ceram. Soc. **89**(8), 2466–2472 (2006). doi:10.1111/j.1551-2916.2006.01114.x
13. T. Kasuga, E. Ueno, A. Obata, Key Eng. Mater. **330–332**, 157–160 (2007)
14. D. Haverty, S. Tofail, K. Stanton, J. McMonagle, Phys. Rev. B **71**(9), 94–103 (2005). doi:10.1103/PhysRevB.71.094103
15. K. Stanton, J. Vanhumbeeck, Adv. Sci. Tech. **45**, 1275–1280 (2006)
16. S. Lopez-Esteban, E. Saiz, S. Fujino, T. Oku, K. Suganuma, A. Tomsia, J. Eur. Ceram. Soc. **23**(15), 2921–2930 (2003). doi:10.1016/S0955-2219(03)00303-0
17. J. Gomez-Vega, E. Saiz, A. Tomsia, G. Marshall, S. Marshall, Biomat. **21**(2), 105–111 (2000). doi:10.1016/S0142-9612(99)00131-3
18. K. Stanton, K. O'Flynn, S. Newcombe, Key Eng. Mater. **361–363**, 269–272 (2007)
19. M. Otten, J. Electron Microsc. Tech. **17**(2), 221–230 (1991). doi:10.1002/jemt.1060170209
20. S. Pennycook, Adv. Imaging Electron Phys. **123**, 173–206 (2002)
21. A. Amali, P. Rez, Microsc. Microanal. **3**(1), 28–46 (2003)
22. G. Winkelman, C. Dwyer, C. Marsh, T. Hudson, D. Nguyen-Manh, M. Döblinger et al., Mater. Sci. Eng. A **422**(1–2), 77–84 (2006). doi:10.1016/j.msea.2006.01.003
23. L. Trentani, F. Pelillo, F. Pavesi, L. Ceciliani, G. Cetta, A. Forlino, Biomater. **23**(14), 2863–2869 (2002). doi:10.1016/S0142-9612(01)00413-6
24. S. Nag, R. Banerjee, J. Stechschulte, H. Fraser, J. Mater. Sci. Mater. Med. **16**(7), 679–685 (2005). doi:10.1007/s10856-005-2540-6
25. K. Stanton, R. Hill, J. Mater. Sci. **35**, 1–6 (2000). doi:10.1023/A:1004710301219
26. K. Stanton, R. Hill, J. Cryst. Growth **275**, 2061–2068 (2005). doi:10.1016/j.jcrysgro.2004.11.266
27. N. Ray, *Inorganic polymers* (Academic Press, New York, 1978)
28. R. Hill, A. Calver, A. Stamboulis, N. Bubb, J. Am. Ceram. Soc. **90**(3), 763–768 (2007). doi:10.1111/j.1551-2916.2006.01474.x
29. R. Hill, A. Calver, S. Skinner, A. Stamboulis, R. Law, Key Eng. Mater. **309–311**, 305–308 (2006)
30. A. Tomsia, J. Pask, Dent. Mater. **2**(1), 10–16 (1986). doi:10.1016/S0109-5641(86)80063-X
31. F. Hong, D. Holland, Surf. Coat. Tech. **39/40**, 19–27 (1989). doi:10.1016/0257-8972(89)90037-6
32. I. Donald, J. Mater. Sci. **28**(11), 2841–2886 (1993). doi:10.1007/BF00354689